

VHF Single-Crystal Silicon Elliptic Bulk-Mode Capacitive Disk Resonators—Part I: Design and Modeling

Zhili Hao, *Member, ASME*, Siavash Pourkamali, *Student Member, IEEE*, and Farrokh Ayazi, *Member, IEEE*

Abstract—This paper, the first of two parts, presents the design and modeling of VHF single-crystal silicon (SCS) capacitive disk resonators operating in their elliptical bulk resonant mode. The disk resonators are modeled as circular thin-plates with free edge. A comprehensive derivation of the mode shapes and resonant frequencies of the in-plane vibrations of the disk structures is described using the two-dimensional (2-D) elastic theory. An equivalent mechanical model is extracted from the elliptic bulk-mode shape to predict the dynamic behavior of the disk resonators. Based on the mechanical model, the electromechanical coupling and equivalent electrical circuit parameters of the disk resonators are derived. Several considerations regarding the operation, performance, and temperature coefficient of frequency of these devices are further discussed. This model is verified in part II of this paper, which describes the implementation and characterization of the SCS capacitive disk resonators. [1223]

Index Terms—Capacitive resonator, disk resonator, electromechanical coupling, elliptic bulk-mode, equivalent electrical circuit, temperature coefficient of frequency.

I. INTRODUCTION

MICROMECHANICAL resonators are of great interest for a wide range of sensing [1], [2] and frequency filtering applications [3], [4]. Studies of micromechanical resonators have mostly targeted the flexural modes of beam and beam-like structures because of their low stiffness and relative ease of excitation and detection. However, it has been observed that the attainable quality factors in beam resonators tend to decrease as the beam size is decreased. As the dimensions are scaled down to achieve higher resonant frequencies, surface loss [5] and support loss [6] are likely to become the dominant dissipation mechanisms in beam resonators due to their high surface-to-volume and small length-to-width ratios.

With the increasing demand for micro- and nanomechanical resonators with very high frequencies and very high-quality factors, disk resonators operating in their ultra-stiff bulk resonant modes become a very attractive alternative to beam resonators. Since the structural stiffness of the bulk modes are typically orders of magnitude larger than that of the flexural modes, high resonant frequencies (in the gigahertz) can be obtained without the need to scale the resonator dimensions into the nanometer

domain. Therefore, bulk-mode resonators are easier to fabricate and alleviate surface loss because of their smaller surface-to-volume ratio compared to that of flexural beam resonators. Recent work has demonstrated that the quality factor of silicon disk resonators operating in their elliptic bulk-mode can be as high as 40 000 at 148 MHz [7] and 98 000 at 73.6 MHz [8].

This paper focuses on the design and modeling of the capacitive disk resonators operating in their elliptic bulk-mode. Using the two-dimensional (2-D) elastic theory, a comprehensive derivation of the in-plane vibrations of the disk structure is first described, providing mathematical expressions for the mode shapes and resonant frequencies. Based on the elliptic bulk-mode shape, the equivalent mechanical parameters of the disk resonator are derived to predict its dynamic behavior. Following that, an equivalent circuit model for the capacitive disk resonator is obtained, providing closed-form expressions for the electromechanical coupling and motional resistance of the resonator. Several considerations regarding the operation, performance, and temperature coefficient of frequency of these devices are further discussed.

II. DESIGN AND OPERATION

Fig. 1 shows a schematic view of a capacitive disk resonator of radius R that is clamped to an anchor through a side-support beam of width b and length L . The capacitive drive and sense electrodes, concentric with the disk, span an equal angle of θ_e and are separated from the disk by capacitive gaps denoted by d_d and d_s for the drive and the sense electrodes, respectively. The resonant structure, consisting of the disk and the support beam, and the electrodes are of the same thickness h . The device is operated in a two-port drive and sense configuration, with a dc polarization voltage V_p applied to the resonant structure. In order to excite the device into resonance, an ac drive voltage signal v_d is applied to the drive electrode, while the sense current signal i_s is detected from the sense electrode. The dc level of both the drive and sense electrodes is at ground.

With origin set at the center of the disk, the plane polar coordinates r and θ is used in this work, as shown in Fig. 1. The disk resonator vibrates in the in-plane elliptic bulk-mode illustrated by the dotted line, which involves both radial and circumferential displacements in the disk. This elliptic bulk-mode has four resonant nodes at the disk periphery, located 90° apart from one another, where the radial displacements diminish. In order to reduce the support loss in the disk, the support beam is located at one of these four resonant nodes, 45° away from the center

Manuscript received December 10, 2003; revised February 9, 2004. This work was supported by the DARPA NMAPS program under Contract DAAH01-01-1-R004. Subject Editor G. Stemme.

The authors are with the School of Electrical and Computer Engineering, Georgia Institute of Technology, Atlanta, GA 30332-0250 USA (e-mail: zhili.hao@ece.gatech.edu).

Digital Object Identifier 10.1109/JMEMS.2004.838387

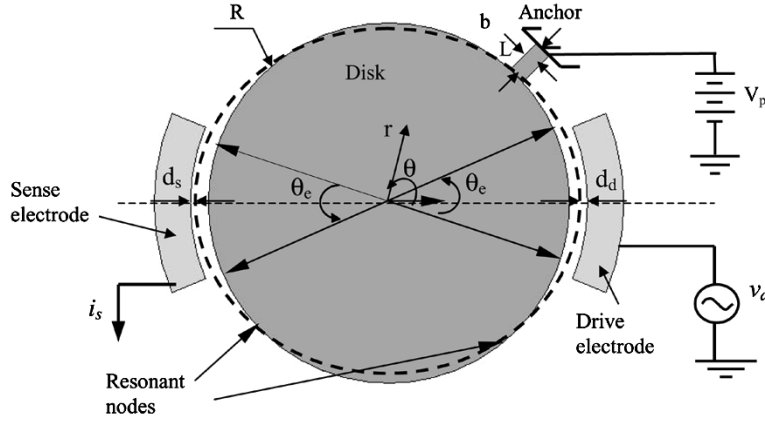


Fig. 1. Schematic view of a capacitive disk resonator with its sense and drive electrodes.

of the drive electrode. In order to excite the elliptic bulk-mode with the maximum electromechanical coupling, the centers of the two electrodes are aligned with the line $\theta = 0^\circ$, where the radial displacements at the edge are maximum. The resonant structure is made of low-resistivity silicon, while the two electrodes are of highly conductive IC-compatible materials such as metal or doped polysilicon [7].

III. IN-PLANE BULK RESONANT MODE OF A DISK

A. Theoretical Derivation

Although some work has been done on the investigation and documentation of the modal characteristics of the in-plane vibrations of disk structures [9]–[12], the resonant frequencies and mode shapes of the in-plane vibrations of a disk are not well documented. This section provides a comprehensive derivation of the in-plane vibrations of a disk to obtain mathematical expressions for the mode shapes and resonant frequencies. It is assumed that the vibration variables are independent of the thickness, and the support beam has negligible effect on the in-plane vibrations of the disk. These assumptions are valid as long as the resonator thickness is much smaller than its diameter and the support beam size is much smaller than the disk size. Thus, the disk is modeled as a circular thin-plate with free edge. For simplicity, it is assumed that the disk resonator is made of an isotropic and homogeneous material. The effect of anisotropy of single crystal silicon on the model will be discussed in the following subsection.

The 2-D elastic theory governing the in-plane vibrations of a disk, in the absence of body forces, may be written in the following format [13]:

$$\frac{E}{1-\nu^2} \cdot \nabla(\nabla \cdot \vec{u}) - \frac{E}{2 \cdot (1+\nu)} \cdot \nabla \times \nabla \times \vec{u} = \rho \cdot \frac{\partial^2 \vec{u}}{\partial t^2} \quad (1)$$

where E , ν , and ρ denote the Young's modulus, Poisson's ratio, and density of the resonator structural material, respectively. The displacement vector \vec{u} may be defined in terms of the pressure-wave (P-wave) scalar potential, Φ , and the shear-wave (S-wave) vector potential, $\vec{\Psi}$, via Helmholtz' theorem as [11]:

$$\vec{u} = \nabla \Phi + \nabla \times \vec{\Psi}. \quad (2)$$

In our case, only the z -coordinate component of $\vec{\Psi}$ along the thickness of the thin-plate (denoted by Ψ) is nonzero, because the vibration variables are independent of the z -coordinate.

By substituting (2) into (1) and taking the divergence and curl of (1), respectively, the elastic equations for the P-wave and S-wave may be written as

$$\frac{\partial^2 \Phi}{\partial t^2} = \alpha^2 \cdot \nabla^2 \Phi \quad (3a)$$

$$\frac{\partial^2 \Psi}{\partial t^2} = \beta^2 \cdot \nabla^2 \Psi \quad (3b)$$

where $\nabla^2 = (1/r) \cdot (\partial/\partial r) + (\partial^2/\partial r^2) + (1/r^2) \cdot (\partial/\partial \theta)$ in polar coordinates; $\alpha = \sqrt{E/\rho(1-\nu^2)}$ and $\beta = \sqrt{E/2\rho(1+\nu)}$ are the propagation velocities of the P-wave and S-wave, respectively.

The solutions to (3) can be expressed as [11]:

$$\Phi_m = A_m \cdot J_m(k_m r/R) \cdot \cos(m\theta) \cdot e^{i\omega_m t} \quad (4a)$$

$$\Psi_m = B_m \cdot J_m(h_m r/R) \cdot \sin(m\theta) \cdot e^{i\omega_m t} \quad (4b)$$

where mode shapes are expressed in terms of the trigonometric and Bessel functions of the first kind (J_m). It has been assumed that m , the mode order, is equal to or larger than 2. It is worth noting that $m = 0$ corresponds to mode shapes that are independent of the circumferential direction, with displacements solely either in the radial direction (radial) or in the circumferential direction (torsional), while $m = 1$ involves nonzero deformation at the center of the disk (translational) [12]. In this work, we consider modes for which $m \geq 2$, as these modes provide resonant nodes on the disk periphery. By locating the support beam at the resonant node of the disk resonator, its support loss is greatly reduced.

In (4), ω_m is the m th angular resonant frequency. A_m and B_m are the constants of the elastic waves, in the unit of squared meter. k_m and h_m are both dimensionless frequency parameters, respectively, expressed as

$$k_m = \omega_m \cdot R/\alpha \quad (5a)$$

$$h_m = \omega_m \cdot R/\beta. \quad (5b)$$

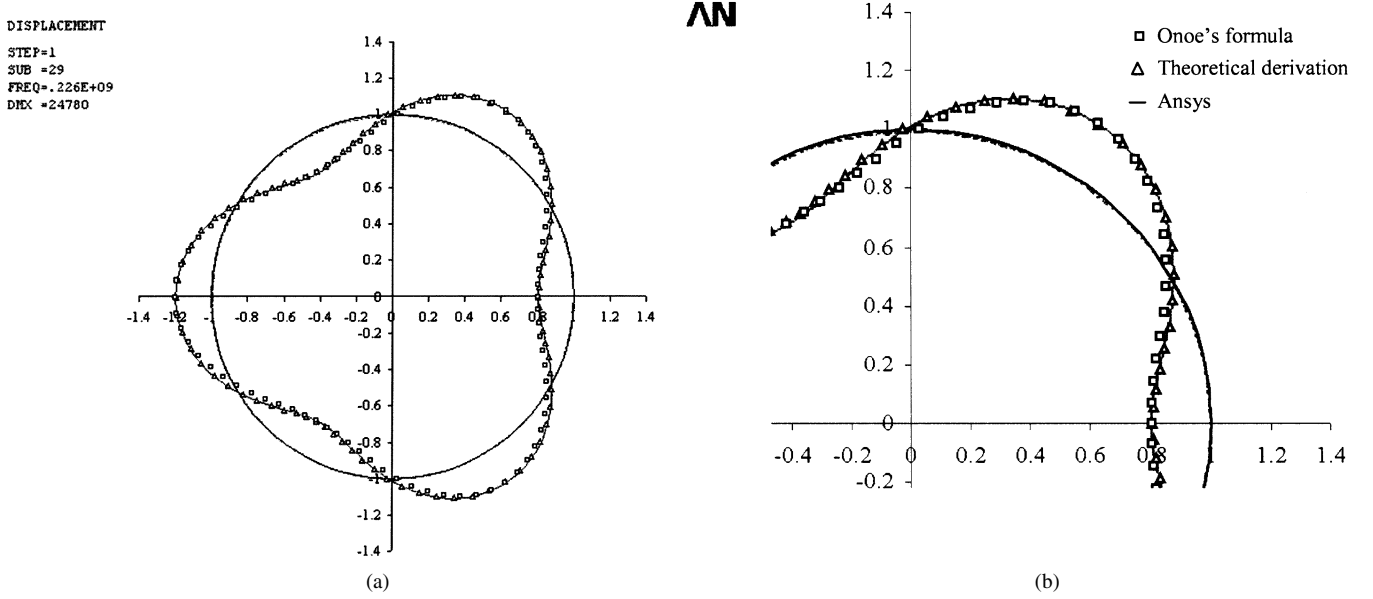


Fig. 2. The third mode shape calculated from the described theoretical derivation (triangles), Morio Onoe's formula (squares), and simulated from ANSYS (solid line), respectively. (a) Theoretical and numerical results. (b) Enlarged portion.

Substituting (4) into (2) leads to the radial (U) and circumferential (V) components of the displacement vector (\vec{u}), respectively, expressed as

$$U_m = \left[A_m \cdot \frac{d}{dr} J_m(k_m r/R) + \frac{m}{r} B_m \cdot J_m(h_m r/R) \right] \cdot \cos(m\theta) \quad (6a)$$

$$V_m = \left[A_m \cdot \frac{-m}{r} J_m(k_m r/R) - B_m \frac{d}{dr} J_m(h_m r/R) \right] \cdot \sin(m\theta). \quad (6b)$$

For a disk with free edge, the boundary conditions at $r = R$ are expressed, in terms of displacements, by the following relations [11]:

$$\sigma_r|_{r=R} = \frac{E}{(1-\nu^2)} \cdot \left[\frac{\partial U}{\partial r} + \frac{\nu}{r} \cdot \left(U + \frac{\partial V}{\partial \theta} \right) \right] = 0 \quad (7a)$$

$$\tau_{r\theta}|_{r=R} = \frac{E}{2 \cdot (1+\nu)} \cdot \left[\frac{\partial V}{\partial r} + \frac{1}{r} \cdot \left(\frac{\partial U}{\partial \theta} - V \right) \right] = 0 \quad (7b)$$

where σ_r and $\tau_{r\theta}$ denote the radial normal stress and circumferential shear stress, respectively. Substituting (6) into the above boundary conditions gives rise to the following equation:

$$\begin{bmatrix} a_{11} & a_{12} \\ a_{21} & a_{22} \end{bmatrix} \cdot \begin{bmatrix} A_m \\ B_m \end{bmatrix} = 0 \quad (8)$$

where the matrix is associated only with k_m , h_m , and ν , while h_m can be expressed as $h_m = k_m \cdot \sqrt{2/(1-\nu)}$, from (5).

In order to obtain nontrivial solutions for A_m and B_m , the determinant of this matrix must be set to zero. It is the eigenvalue (frequency parameter, k_m) causing the determinant to vanish

that corresponds to the resonant frequency of the in-plane vibrations of the disk. Therefore, the eigenvalue equation for the resonant frequency can be expressed as (9), shown at the bottom of the page.

From (8), the ratio between the constants of Φ_m and Ψ_m is calculated as:

$$\xi_m = \frac{B_m}{A_m} = \frac{J_m(k_m)}{J_m(h_m)} \cdot \frac{2 \cdot \frac{k_m \cdot J_{m-1}(k_m)}{J_m(k_m)} + h_m^2 - 2m(m+1)}{\left[\frac{h_m \cdot J_{m-1}(h_m)}{J_m(h_m)} - (m+1) \right] \cdot 2m}. \quad (10)$$

The eigenvalue (9) and the ratio (10) are both solely functions of the Poisson's ratio of the resonator structural material. It should be noted that (9) provides the same resonant frequency as what obtained by Onoe [10]; however, the mode shape obtained by Onoe [10] is different from (10). Fig. 2 illustrates the third mode shapes calculated from the above theoretical derivation and Onoe's formula, along with the simulated mode shape for comparison. This figure illustrates that (10) is more accurate in describing the mode shape than Onoe's formula. It should be noted that only when the vibration amplitude of the bulk-modes is very large, noticeable is the difference in the predicted mode shapes between the presented derivation and Onoe's formula.

The resonant frequencies can be calculated from (5a) and are expressed as

$$f_m = \frac{k_m}{2\pi R} \cdot \sqrt{\frac{E}{\rho \cdot (1-\nu^2)}} \quad (11)$$

where $m = 2, 3, \dots$, and k_m is determined by (9).

$$\left[\frac{k_m \cdot J_{m-1}(k_m)}{J_m(k_m)} - m - \frac{h_m^2}{2(m^2-1)} \right] \cdot \left[\frac{h_m \cdot J_{m-1}(h_m)}{J_m(h_m)} - m - \frac{h_m^2}{2(m^2-1)} \right] - m^2 \cdot \left(\frac{h_m^2}{2(m^2-1)} - 1 \right)^2 = 0. \quad (9)$$

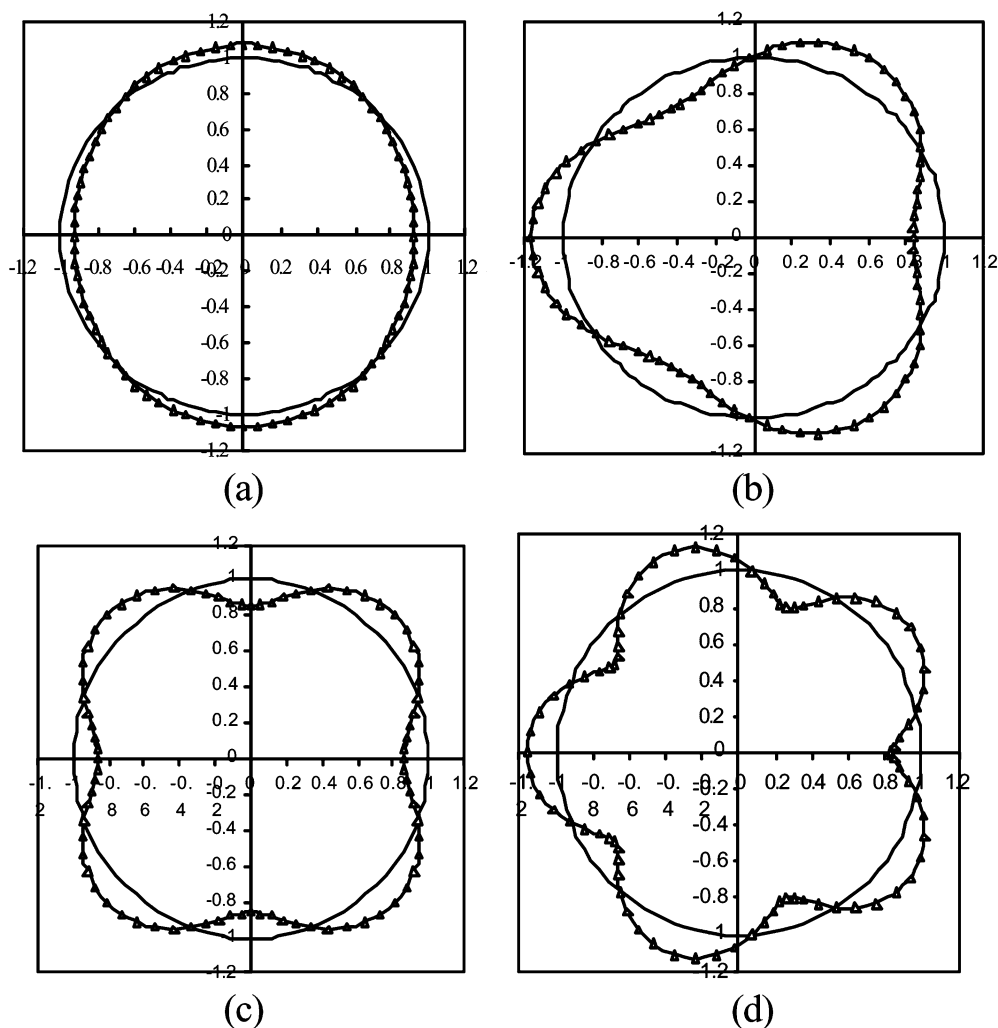


Fig. 3. Mode shapes calculated from the theoretical derivation with triangles symbolizing the vibration modes. (a) $m = 2$, (b) $m = 3$, (c) $m = 4$, (d) $m = 5$.

TABLE I
THE RELATED ELLIPTIC BULK-MODE PARAMETERS FOR A DISK RESONATOR. THE SUBSCRIPT $m = 2$ IS OMITTED

Materials	Single crystal silicon $\langle 110 \rangle$	Single crystal silicon $\langle 100 \rangle$	Polysilicon	GaAs
Poisson's ratio (ν)	0.064	0.279	0.22	0.31
Frequency parameter (k)	1.6002	1.4082	1.4638	1.3780
Ratio (ξ)	-2.1920	-2.1865	-2.2144	-2.1630
Dimensionless maximum radial displacement at the edge (U_R)	-1.4469	-1.4984	-1.5047	-1.4883
Dimensionless circumferential displacement at resonant nodes (V_R)	0.3719	0.4613	0.4459	0.4662
Integral for the kinetic energy (Σ)	0.7522	0.8272	0.8294	0.8183
Effective mass Coefficient (Σ/U_R^2)	0.3593	0.3684	0.3663	0.3694

By solving for eigenvalues in (9) using any available mathematical software, resonant frequencies and mode shapes can be obtained. Several mode shapes are depicted in Fig. 3 to illustrate the in-plane vibration behavior. It should be noted that, for isotropic and homogeneous disk resonators, each vibration mode is accompanied by its degenerate mode with the same corresponding resonant frequency while $90^\circ/m$ apart in the circumferential direction, in that the cosine and sine functions in Φ_m and Ψ_m are exchangeable.

As illustrated in Fig. 3, the elliptic bulk-mode corresponds to the in-plane vibration mode of $m = 2$. The related elliptic bulk-mode parameters calculated from this theoretical derivation are listed in Table I for several typical structural materials used in fabrication of micromechanical resonators, where the material properties of single crystal silicon (SCS) along both the $\langle 110 \rangle$ and $\langle 100 \rangle$ orientations are used [14]. Some of the parameters listed in Table I will be described later in the paper.

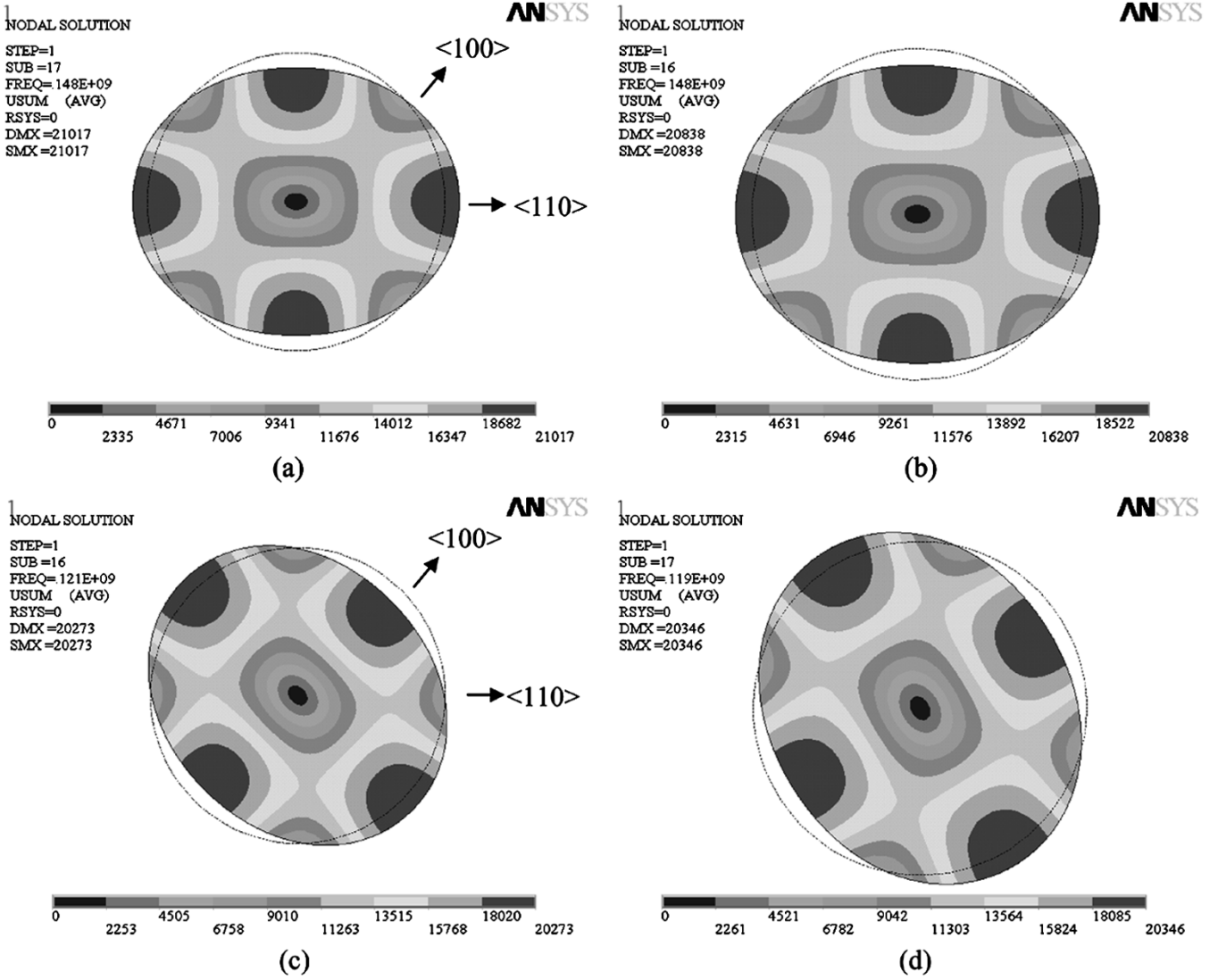


Fig. 4. Elliptic bulk-mode from numerical simulation of a disk of diameter $29.4 \mu\text{m}$ and thickness $3 \mu\text{m}$, supported at its center, with the anisotropic and isotropic material properties of single crystal silicon. Legend shows the relative displacement distribution across the disk resonator and solid line denotes the undeformed shape. (a) Anisotropic material properties, $f = 148 \text{ MHz}$ elliptic bulk-mode in operation. (b) Isotropic material properties along the $\langle 110 \rangle$ orientation $f = 148 \text{ MHz}$ ($E = 169 \text{ GPa}$, $\nu = 0.064$). (c) Anisotropic material properties, $f = 121 \text{ MHz}$ degenerate elliptic bulk-mode. (d) Isotropic material properties along the $\langle 100 \rangle$ orientation $f = 119 \text{ MHz}$ ($E = 130 \text{ GPa}$, $\nu = 0.279$).

B. Numerical Simulation

To verify the theoretical derivation of the elliptic bulk-modes, numerical simulation is performed using ANSYS on a disk resonator of diameter $29.4 \mu\text{m}$ and thickness $3 \mu\text{m}$ fabricated in Part II of this paper. In order to investigate the effect of the support beam on the vibrations of the disk resonator, two types of support for the SCS disk resonator are simulated: 1) supported at its center (using a very small support post), and 2) side-supported at its edge by a support beam (width $1.7 \mu\text{m}$ and length $2.7 \mu\text{m}$).

Fig. 4 shows the simulated elliptic bulk-modes of the disk of diameter $29.4 \mu\text{m}$ supported at its center. Fig. 4(a) and (c) shows the two degenerate elliptic bulk-modes simulated in SCS (45° apart) for which the anisotropic material properties of SCS were used. The difference in the resonant frequencies of these two modes is introduced due to the anisotropy of the Young's modulus of SCS. On the other hand, Fig. 4(b) and (d) shows

the elliptic bulk modes in an isotropic material having identical parameters corresponding to the $\langle 110 \rangle$ and $\langle 100 \rangle$ directions in SCS, respectively. For the isotropic material properties, the difference in the resonant frequencies obtained through our theoretical derivation and numerical simulation is less than 0.1% . The comparison of Fig. 4(a) to (b) and Fig. 4(c) to (d) indicates that the resonant frequency of the SCS disk in the elliptic bulk-mode of interest can be calculated using the material properties along the $\langle 110 \rangle$ orientation, while the resonant frequency of the degenerate mode can be calculated using the material properties along the $\langle 100 \rangle$ orientation. This may be explained by that the displacement in these vibration modes mainly happens along the $\langle 110 \rangle$ and $\langle 100 \rangle$ orientation, as illustrated in Fig. 4. Hence, the effect of the anisotropy of SCS on the elliptic bulk-modes is negligible. For the elliptical bulk-mode of interest, it is reasonable to treat the SCS disk resonator as an isotropic material having the $\langle 110 \rangle$ material properties of SCS. The analytical treatment of the anisotropy of SCS to ob-

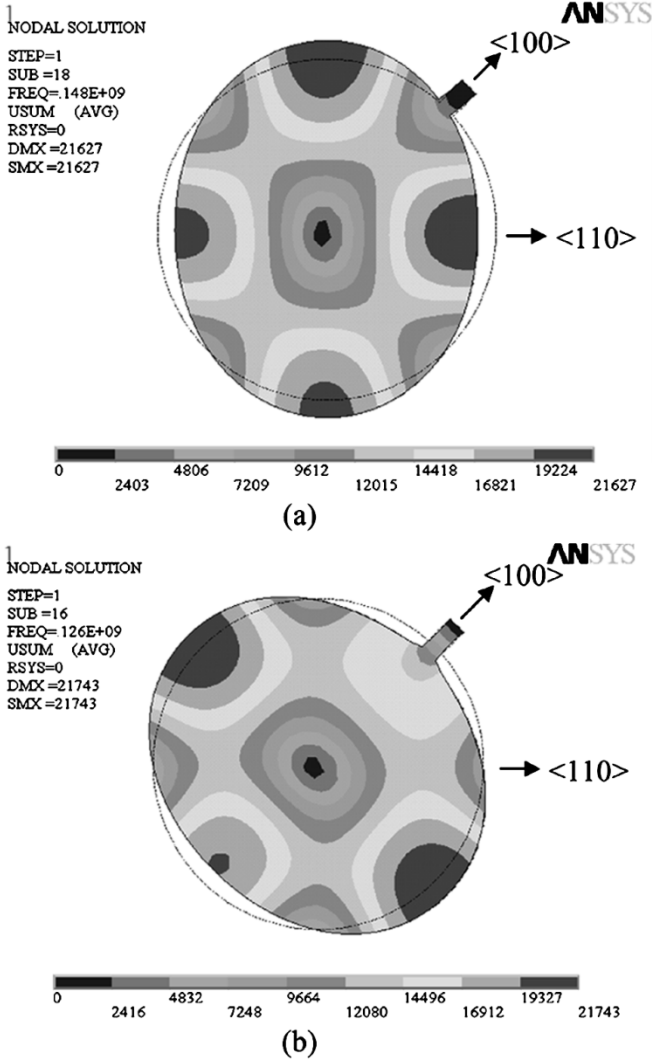


Fig. 5. Elliptic bulk-mode shape ($m = 2$) from numerical simulation of a side-supported disk of diameter $29.4 \mu\text{m}$ and thickness $3 \mu\text{m}$, with the anisotropic material properties of single crystal silicon used in the simulation. The support beam (width $1.7 \mu\text{m}$ and length $2.7 \mu\text{m}$) is oriented along the $\langle 100 \rangle$ orientation. Legend shows the relative displacement distribution across the disk resonator and solid line denotes the undeformed shape. (a) Elliptic bulk-mode in operation $f = 148$ MHz. (b) Degenerate elliptic mode $f = 126$ MHz.

tain closed-form expressions for resonant frequencies and mode shapes is very difficult, if not impossible [15].

Fig. 5 shows the simulated elliptic bulk-mode shapes of a side-supported SCS disk of diameter $29.4 \mu\text{m}$. The anisotropic material properties of single crystal silicon are used in this simulation and the support beam is oriented along the $\langle 100 \rangle$ orientation (similar to the fabricated SCS disk of part II). Comparison between Figs. 4 and 5 shows that the support beam has negligible effect on both the frequency and mode shape of the elliptic bulk-mode in operation (148 MHz). However, the effect of the support beam on the degenerate elliptic bulk-mode is noticeable. The slight increase in the frequency may be explained by that the support beam is located at a position, where the maximum radial displacement for the degenerate bulk-mode occurs, making the structure much stiffer.

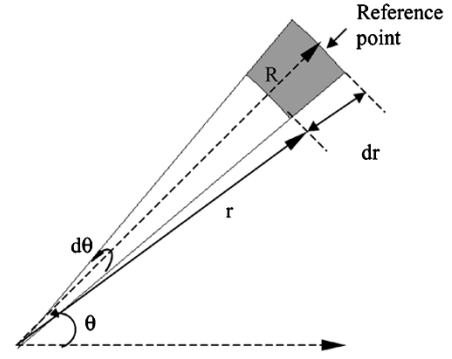


Fig. 6. An infinitesimal element $d\theta$ along the circumferential direction θ .

IV. ELECTROMECHANICAL MODEL

A. Equivalent Mechanical Model

In general, an equivalent mechanical model can be used to describe the dynamic behavior of the disk resonator operating in its elliptic bulk-mode. The following describes the procedure of extracting this equivalent model. In the rest of the paper, the subscript “2” representing the second mode is omitted for simplicity, since the disk operates in its elliptic bulk-mode in this work. However, similar analysis can be applied to higher order modes to derive their electromechanical model.

Since the excitation and detection of this disk resonator is mainly through the gap variation along the radial direction, only the vibration variables along the radial direction are considered here. Through combining (6) and (10), the radial displacement at the location (r, θ) can be rewritten as

$$U = \frac{A}{R} \cdot \cos(2\theta) \cdot U_r \quad (12)$$

where

$$U_r = k \cdot J_1(kr') - \frac{2}{r'} \cdot J_2(kr') + \frac{2}{r'} \cdot \xi \cdot J_2(hr') \quad (13)$$

$r' = r/R$ denotes the dimensionless radial coordinate, normalized to the disk radius R . As illustrated in Fig. 6, with an infinitesimal disk edge along the circumferential direction, θ , as the reference point, the effective mass for an infinitesimal element, $d\theta$, can be expressed as [16]:

$$m(\theta) = \rho \cdot h \cdot R^2 \cdot \Sigma / U_R^2 \cdot d\theta \quad (14)$$

where $\Sigma = \int_0^1 U_r^2 \cdot r' \cdot dr'$ is the integral for the kinetic energy and $U_R = k \cdot J_1(k) - 2 \cdot J_2(k) + 2 \cdot \xi \cdot J_2(h)$ is the dimensionless maximum radial displacement at the disk edge. As the functions of solely the Poisson's ratio of the material used, both Σ and U_R are listed in Table I.

The dynamic behavior of this infinitesimal element along the circumferential direction, θ , can be described by the second-order equation of motion, shown in (15) at the bottom of the next page, where c_d is the damping-related coefficient for this element and $f_e(\theta)$ is the radial electrostatic force per unit radian from the drive and sense electrodes. Multiplying (15) by the mode shape of $\cos(2\theta) \cdot U_R$ [17], [18] and integrating both

sides of this equation, from 0 to 2π , gives rise to (16), shown at the bottom of the page, where A/R and C_d are the radial vibration amplitude and damping coefficient of the disk resonator, respectively. $\omega = 2\pi f$ is the angular frequency of the elliptic bulk-mode. Hence, the equivalent mass and equivalent stiffness are, respectively, expressed as

$$M = \pi \cdot \rho \cdot h \cdot R^2 \cdot \Sigma / U_R^2 \quad (17)$$

$$K = M \cdot \omega^2 \quad (18)$$

where Σ / U_R^2 denotes the effective mass coefficient, as listed in Table I.

Since the capacitive gap is extremely small compared with the disk radius, the capacitances for the drive and sense electrodes can be calculated using a parallel-plate model. Thus, the electrostatic excitation force per unit radian from the drive and sense electrodes, respectively, can be calculated as

$$f_d(\theta) = \frac{1}{2} \cdot \frac{\varepsilon \cdot h \cdot R}{d_d^2} \cdot \left\{ -2 \cdot V_p \cdot v_d + 2 \cdot \frac{A}{R} \cdot \frac{U_R \cdot \cos(2\theta)}{d_d} \cdot V_p^2 \right\} \quad (19)$$

$$f_s(\theta) = \frac{1}{2} \cdot \frac{\varepsilon \cdot h \cdot R}{d_s^2} \cdot \left\{ 2 \cdot \frac{A}{R} \cdot \frac{U_R \cdot \cos(2\theta)}{d_s} \cdot V_p^2 \right\} \quad (20)$$

where d_d and d_s are the capacitive gaps for the drive and the sense electrodes, respectively, and ε denotes the permittivity of air.

Substituting the above two equations into (16) gives rise to the equivalent electrostatic stiffness and the equivalent force for the elliptic bulk-mode, respectively, expressed as

$$K_e = \varepsilon \cdot h \cdot R \cdot \left(\frac{\theta_e}{2} + \frac{\sin(2\theta_e)}{4} \right) \cdot V_p^2 \cdot \left\{ \frac{1}{d_d^3} + \frac{1}{d_s^3} \right\} \quad (21)$$

$$F = \frac{\varepsilon \cdot h \cdot R}{d_d^2 \cdot U_R} \cdot (-V_p \cdot v_d) \cdot \sin(\theta_e). \quad (22)$$

Hence, the equivalent mechanical model for describing the dynamic behavior of the disk resonator can be further expressed as

$$M \cdot \frac{d^2}{dt^2} \left[\frac{A}{R} \right] + C_d \frac{d}{dt} \left[\frac{A}{R} \right] + (K - K_e) \cdot \frac{A}{R} = F. \quad (23)$$

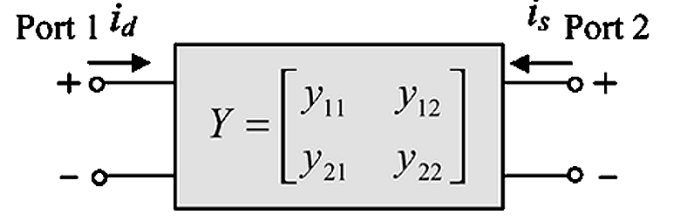


Fig. 7. Y-parameter representation of the two-port electrical circuit model.

Taking into account the tuning effect of the polarization voltage through combining (21) and (23), the resonant frequency of this device can be calculated by (24) at the bottom of the page.

It can be seen from (24) that the frequency-tuning capability of the device strongly depends on the capacitive gaps and the polarization voltage. Since fabrication tolerances are unavoidable, it is necessary to tune the frequencies of the disk resonators when deployed as arrays. As the disk scales down for higher frequencies with the other design parameters fixed, its frequency-tuning capability is decreased. In order to maintain certain frequency-tuning capability, it is required that either the capacitive gaps be decreased or the polarization voltage be increased. It is worth noting that these two design parameters are limited by linearity in the vibrations.

B. Equivalent Circuit Model

As shown in Fig. 7, the two-port electrical equivalent circuit model for the disk resonator can be developed by the derivation of its four Y-parameters (admittance parameters), which are defined as the ratio of the current measured at one port to the drive voltage at the same or the other port while the undriven port of the circuit is shorted to ground expressed as [19]:

$$\begin{aligned} Y_{11}(j\omega) &= \left. \frac{i_d(j\omega)}{v_d(j\omega)} \right|_{v_s=0}, & Y_{12}(j\omega) &= \left. \frac{i_d(j\omega)}{v_s(j\omega)} \right|_{v_d=0} \\ Y_{21}(j\omega) &= \left. \frac{i_s(j\omega)}{v_d(j\omega)} \right|_{v_s=0}, & Y_{22}(j\omega) &= \left. \frac{i_s(j\omega)}{v_s(j\omega)} \right|_{v_d=0} \end{aligned} \quad (25)$$

$$\left\{ m(\theta) \cdot \frac{d^2}{dt^2} \left[\frac{A}{R} \cdot U_R \right] + c_d \cdot \frac{d}{dt} \left[\frac{A}{R} \cdot U_R \right] + K(\theta) \cdot \left[\frac{A}{R} \cdot U_R \right] \right\} \cdot \cos(2\theta) = f_e(\theta) \quad (15)$$

$$\pi \cdot \rho \cdot h \cdot R^2 \cdot \frac{\Sigma}{U_R^2} \cdot \frac{d^2}{dt^2} \left[\frac{A}{R} \right] + C_d \frac{d}{dt} \left[\frac{A}{R} \right] + \pi \cdot \rho \cdot h \cdot R^2 \cdot \frac{\Sigma}{U_R^2} \cdot \omega^2 \cdot \frac{A}{R} = \frac{1}{U_R} \cdot \int_0^{2\pi} f_e(\theta) \cdot \cos(2\theta) \cdot d\theta \quad (16)$$

$$f_{\text{tuned}} = f \cdot \sqrt{1 - \varepsilon \cdot h \cdot R \cdot \left(\frac{\theta_e}{2} + \frac{\sin(2\theta_e)}{4} \right) \cdot V_p^2 \cdot [1/d_d^3 + 1/d_s^3] / K}. \quad (24)$$

where i_s, v_s, i_d , and v_d are the current and voltage measured at the sense electrode (Port 2) and drive electrode (Port 1), respectively.

For the micromechanical resonators, the admittance parameter can be further expressed in terms of the mechanical force-displacement transfer function for the disk resonator, $Z(j\omega)/F(j\omega)$, and the electromechanical coupling at the input and output ports, η_1, η_2, η'_1 , and η'_2 . Here, the displacement Z denotes the vibration amplitude A/R . The input and output coupling terms are expressed as

$$\eta_1(j\omega) = \frac{F(j\omega)}{v_d(j\omega)} \quad (26)$$

$$\eta_2(j\omega) = \frac{Q_s(j\omega)}{Z(j\omega)} = \frac{1}{j \cdot \omega} \cdot \frac{i_s(j\omega)}{Z(j\omega)} \quad (27)$$

$$\eta'_1(j\omega) = \frac{Q_d(j\omega)}{Z(j\omega)} = \frac{1}{j \cdot \omega} \cdot \frac{i_d(j\omega)}{Z(j\omega)} \quad (28)$$

$$\eta'_2(j\omega) = \frac{F(j\omega)}{v_s(j\omega)} \quad (29)$$

where Q_s and Q_d are the charge going through the sense and drive electrode, respectively. While the electromechanical coupling from the drive electrode to the sense electrode is denoted by η_1 and η_2 , the coupling from the sense electrode to the drive electrode is denoted by η'_1 and η'_2 .

Through combining the above equations, Y_{11} and Y_{21} can be rewritten as [17]

$$Y_{11}(j\omega) = \frac{Z(j\omega)}{F(j\omega)} \cdot \frac{F(j\omega)}{v_d(j\omega)} \cdot \frac{i_d(j\omega)}{Z(j\omega)} = j \cdot \omega \cdot \frac{Z(j \cdot \omega)}{F(j \cdot \omega)} \cdot \eta_1 \cdot \eta'_1 \quad (30)$$

$$Y_{21}(j\omega) = \frac{Z(j\omega)}{F(j\omega)} \cdot \frac{F(j\omega)}{v_d(j\omega)} \cdot \frac{i_s(j\omega)}{Z(j\omega)} = j \cdot \omega \cdot \frac{Z(j \cdot \omega)}{F(j \cdot \omega)} \cdot \eta_1 \cdot \eta_2 \quad (31)$$

From (23), the force-displacement transfer function of the disk resonator can be expressed as

$$\frac{Z(j\omega)}{F(j\omega)} = \frac{\frac{1}{K \cdot j\omega}}{\frac{j\omega}{\omega^2} + \frac{1}{\omega \cdot Q} + (1 - K_e/K) \cdot \frac{1}{j\omega}} \quad (32)$$

where Q is the quality factor of the disk resonator.

Substituting (22) into (26) and (29) gives rise to the following expressions for the voltage-force transfer functions at the sense and drive electrodes:

$$\eta_1(j\omega) = \frac{\varepsilon \cdot h \cdot R}{d_d^2 \cdot U_R} \cdot (-V_p) \cdot \sin(\theta_e) \quad (33)$$

$$\eta'_2(j\omega) = \frac{\varepsilon \cdot h \cdot R}{d_s^2 \cdot U_R} \cdot (-V_p) \cdot \sin(\theta_e). \quad (34)$$

The displacement-current transfer functions at the sense and drive electrodes can be written as:

$$\eta'_1(j\omega) = \frac{\varepsilon \cdot h \cdot R}{d_d^2} \cdot U_R \cdot \sin(\theta_e) \cdot (-V_p) \quad (35)$$

$$\eta_2(j\omega) = \frac{\varepsilon \cdot h \cdot R}{d_s^2} \cdot U_R \cdot \sin(\theta_e) \cdot (-V_p). \quad (36)$$

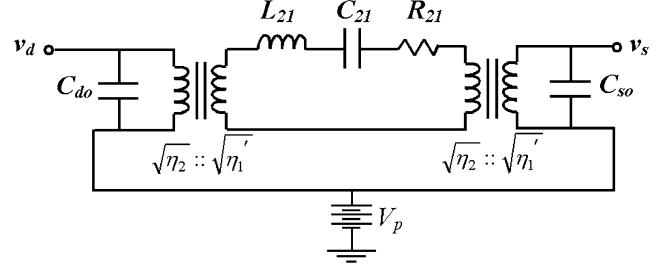


Fig. 8. The equivalent circuit model for a capacitive disk resonator consisting of a series RLC tank terminated with two transformers at the input and output ports counting for asymmetry between the two electrodes.

Substituting (32) to (36) into (30) and (31) results in the transfer functions in the form of admittance of series RLC tanks with the equivalent inductance, capacitance, and resistance expressed, respectively, as

$$L_{21} = \frac{K}{\eta_1 \cdot \eta_2 \cdot \omega^2}, \quad L_{11} = \frac{K}{\eta_1 \cdot \eta'_1 \cdot \omega^2} \quad (37)$$

$$C_{21} = \frac{\eta_1 \cdot \eta_2}{K \cdot (1 - K_e/K)}, \quad C_{11} = \frac{\eta_1 \cdot \eta'_1}{K \cdot (1 - K_e/K)} \quad (38)$$

$$R_{21} = \frac{\sqrt{K \cdot M}}{Q \cdot \eta_1 \cdot \eta_2}, \quad R_{11} = \frac{\sqrt{K \cdot M}}{Q \cdot \eta_1 \cdot \eta'_1} \quad (39)$$

where R_{21} is commonly referred to as the motional resistance.

Following the same procedure, Y_{12} and Y_{22} can be derived, expressed as

$$Y_{12} = Y_{21} = Y_{11} \frac{\eta_2}{\eta'_1} = Y_{22} \frac{\eta'_1}{\eta_2}. \quad (40)$$

Finally, since the two transadmittance parameters (Y_{12} and Y_{21}) are equal and in the form of the admittance of a series RLC tank, the equivalent circuit model includes a series RLC connecting the two ports. On the other hand, the input and output admittances (Y_{11} and Y_{22}) have the same transfer functions as the trans-admittance parameters scaled by the constant factors, (η_2/η'_1) and (η'_1/η_2) . Adding transformers with the same transformation ratios ($\sqrt{\eta_2} : \sqrt{\eta'_1}$) to the input and output ports of the RLC tank, will scale the input and output impedances to the required values without changing the transadmittance parameters. Therefore, the equivalent circuit model shown in Fig. 8 has all the admittance parameters derived for the resonators and can be used for describing the dynamic behavior of the disk resonator. C_{do} and C_{so} are the static capacitances of the drive and sense electrodes, respectively. It is worth mentioning that when interconnect pads are added to the input and output of the resonator, the capacitances related to the pads should be included in C_{do} and C_{so} .

It is worth mentioning that depending on the electrode configuration, the output current can be in phase or 180° out of phase with respect to the input voltage. In case of in phase displacement of the resonator toward sense and drive electrodes, i.e., confronting sense and drive electrodes, the current coming out of the device has a 180° phase difference with the input voltage while for the four-electrode configuration presented in part II of this paper, the output current is in phase with the input voltage.

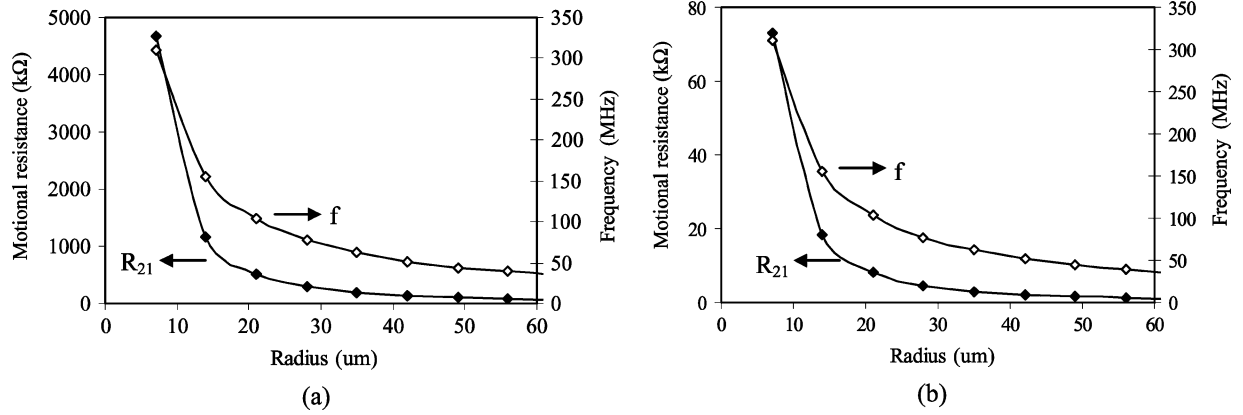


Fig. 9. Characteristics of the motional resistance R_{21} and resonant frequency f versus the disk radius for a disk resonator. (a) $Q = 10000$, $d = 100$ nm, $V_p = 20$ V, $h = R/10$. (b) $Q = 40000$, $d = 25$ nm, $V_p = 5$ V, $h = R/10$.

Fig. 9 shows the characteristics of the motional resistance and resonant frequency versus the disk radius. As the disk scales down for higher frequencies from 30 to 300 MHz, the motional resistance increases dramatically, from 50 K Ω to 4.5 M Ω for $Q = 10000$, $d = 100$ nm, $V_p = 20$ V, $h = R/10$, while from 1 K Ω to 70 K Ω for $Q = 40000$, $d = 25$ nm, $V_p = 5$ V, $h = R/10$. In order to lower this resistance, it is required that the gap d be decreased while the quality factor Q and the polarization voltage V_p be increased.

V. DISCUSSION

A. Electrode Shaping

The shapes of the drive and sense electrodes are critical to the operation of the disk resonator in the elliptic bulk-mode. First, excitation of unwanted modes may be avoided by shaping the driving electrode with respect to a particular vibration mode [18]. As illustrated in Fig. 5, the elliptic bulk-mode in operation is accompanied by its degenerate mode approximately 45° apart in the circumferential direction. The shape of the drive electrode, symmetric to the line $\theta = 0^\circ$, contributes to suppress this degenerate mode. It is worth mentioning that the excitation of this degenerate mode is also constrained by its low quality factor (larger support loss caused by the normal stress of the support beam) and different frequency value caused by the anisotropy of SCS (as it was explained earlier). Second, the maximum frequency-tuning capability is expected from this device in order to achieve certain frequency accuracy. Therefore, the span angle θ_e of the drive and sense electrodes should be maximized. Finally, both stronger electromechanical coupling and lower motional resistance are desirable from these resonators, requiring the span angle to be maximized.

As shown in Fig. 10, when the circumferential direction is away from $\theta = 0^\circ$, the radial displacement at the disk edge decreases while the circumferential displacement increases. Although the increase of the span angle from 0° to 90° will improve the above-mentioned performance, this device may suffer from spatial perturbation incurred by the circumferential

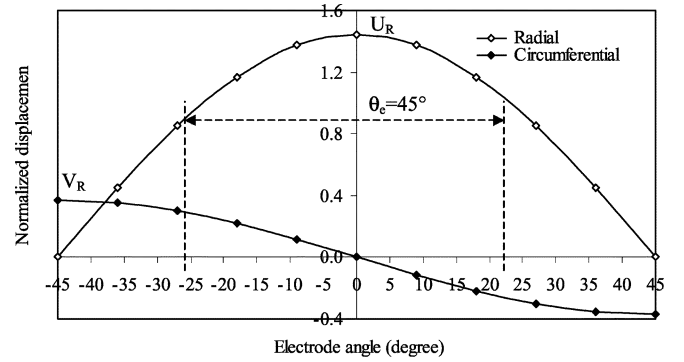


Fig. 10. The characteristics of the radial and circumferential displacement at the disk edge versus the angle, θ .

displacement. Therefore, the span angles of the electrodes are chosen to be 45° in this work.

B. Support Beams

Although the support beam has negligible effect on the resonant frequency of the disk in Section III, the effect of this beam on support loss should be addressed. As illustrated in Fig. 11, while the support beam is located at the resonant node with the radial displacement diminishing, the circumferential displacement at this node is nonnegligible, which can be expressed as

$$V_s = V_R \cdot \frac{A}{R} \quad (41)$$

where $V_R = -2 \cdot J_2(k) - \xi \cdot (h \cdot J_1(h) - 2 \cdot J_2(h))$ is the dimensionless circumferential displacement at resonant nodes, as listed in Table I. It is this circumferential displacement that causes the shear stress at the anchor, further inducing the energy loss to the environment through exciting elastic waves [6]. This theoretical explanation elucidates the experimental observation that the disk resonators with more support beams have lower

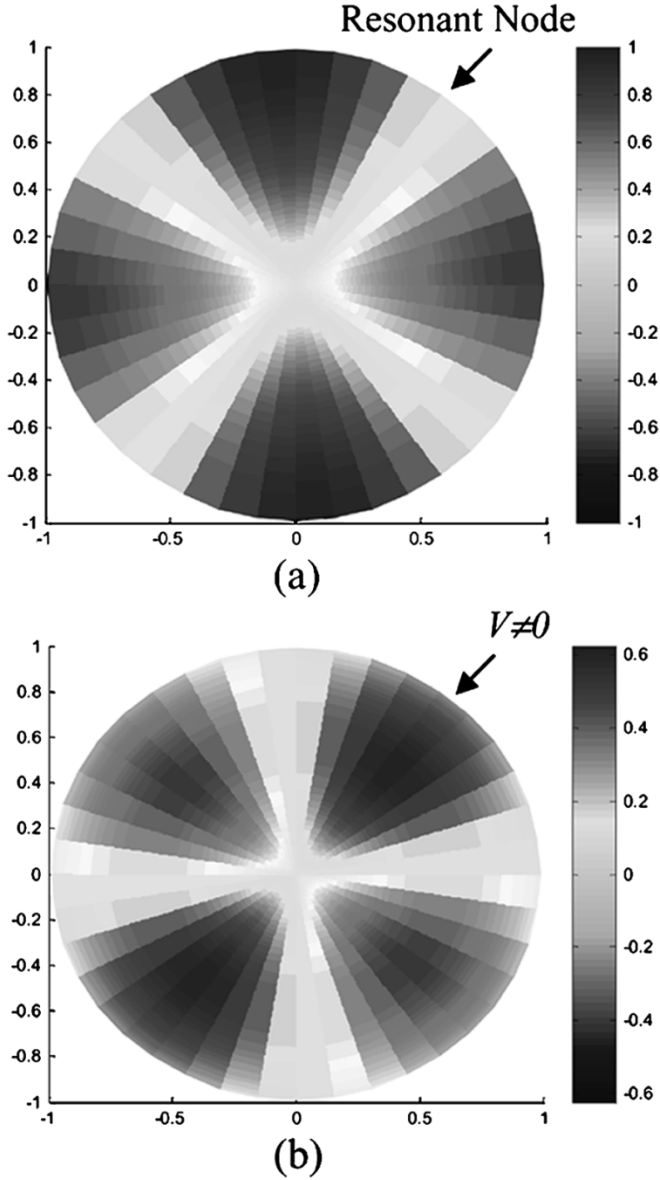


Fig. 11. Normalized radial and circumferential displacement in the elliptic bulk-mode ($m = 2, \nu = 0.064$) calculated from (6). (a) Normalized radial displacement. (b) Normalized circumferential displacement.

quality factors than those of the same sizes with one support beam [7], [8].

C. Temperature Coefficient of Frequency

The resonant frequency of the capacitive disk resonator varies with temperature due to: 1) temperature dependency of the Young's modulus of the resonator structural material; 2) thermal expansion of the material, causing a change in the dimension of the resonator; and 3) variation in the capacitive

gap sizes, causing the variation in the electrostatic stiffness and consequently the resonant frequency of the resonator with temperature. As shown in the previous section, considering the electrostatic stiffness, the resonant frequency for the elliptical bulk-mode of the disk resonator can be written as (42), shown at the bottom of the page.

By taking the derivative of the above expression with temperature T , the temperature coefficient of frequency for the disk resonator can be expressed as

$$\frac{1}{f} \cdot \frac{\partial f}{\partial T} = \frac{1}{2} \alpha_E + \frac{1}{2} \cdot \alpha_T - 3\epsilon \cdot h \cdot R \cdot \theta_e \cdot V_p^2 \cdot \frac{1}{d_d^3} \frac{d(d_d)}{dT} \quad (43)$$

where α_E and α_T denote the temperature coefficient of the Young's modulus and the linear thermal expansion coefficient of the resonator material. It is also assumed that the two capacitive gaps are the same. The last term in this equation shows the effect of temperature-induced variation in the capacitive gaps on the resonant frequency.

From the typical value of ~ 3 ppm/ $^{\circ}\text{C}$ for the linear thermal expansion coefficient of SCS [20], the contribution of this factor to the frequency variation will be ~ 1.5 ppm/ $^{\circ}\text{C}$. Using the thermal expansion coefficient values given in [21] for polysilicon, the gap related frequency variation is in the range of 10^{-4} ppm/ $^{\circ}\text{C}$ for a disk resonator of $29.4 \mu\text{m}$ in diameter with 120 nm capacitive gaps and polarization voltage of 10 V. Comparing with the thermal expansion, the capacitive gaps have negligible effects on the frequency variation.

The measured temperature coefficient of the Young's modulus of SCS as reported so far is much larger than the thermal expansion coefficient of SCS [22]–[24], ranging from -52 ppm/ $^{\circ}\text{C}$ [22] to -100 ppm/ $^{\circ}\text{C}$ [23]. Hence, the frequency drift due to temperature variations mainly results from the temperature dependency of the Young's modulus. It has been found that doping has substantial effect on the temperature coefficient of the Young's modulus of SCS [24]. The disk resonator in this work is made from highly p-type doped single crystal silicon. Therefore, the temperature dependency of the Young's modulus of the silicon resonator can be extracted by fitting the measured temperature coefficient of frequency to (43), [25].

VI. CONCLUSION

Design and modeling of single crystal silicon capacitive disk resonators operating in elliptic bulk-mode are presented. Using the 2-D elastic theory, the elliptic bulk-mode shape and its frequency are derived and verified by the corresponding numerical simulation. Based on the elliptic bulk-mode shape, both the

$$f_{\text{tuned}} = \frac{1.6002}{2\pi R} \cdot \sqrt{\frac{E}{\rho \cdot (1 - \nu^2)}} \cdot \sqrt{1 - \epsilon \cdot h \cdot R \cdot \left[\frac{\theta_e}{2} + \frac{\sin(2\theta_e)}{4} \right] \cdot V_p^2 \cdot [1/d_d^3 + 1/d_s^3] / K}. \quad (42)$$

equivalent mechanical model and electrical circuit model for the disk resonators are extracted to predict their dynamic behavior and provide closed-form expressions for their electromechanical coupling and motional resistance. The effect of electrode shaping and support beams on the operation and performance of these devices is further discussed. Temperature coefficient of frequency for the disk resonators is also addressed. The experimental verification of this modeling work is described in Part II.

ACKNOWLEDGMENT

The authors would like to thank G. Ho and R. Abdolvand for discussions and collaborations.

REFERENCES

- [1] G. Stemme, "Resonant Silicon sensors," *J. Micromech. Microeng.*, vol. 1, pp. 113–125, 1991.
- [2] H. A. C. Tilmans, M. Elwespoeck, and J. H. J. Fluitman, "Micro resonant force gauges," *Sens. Actuators: A, Phys.*, vol. 30, pp. 35–53, 1992.
- [3] S. Pourkamali, A. Hashimura, R. Abdolvand, G. K. Ho, A. Erbil, and F. Ayazi, "High-Q single crystal silicon HARPSS capacitive beam resonators with self-aligned sub-100 nm transduction gaps," *J. Microelectromech. Syst.*, vol. 12, pp. 487–496, Aug. 2003.
- [4] K. Wang, A.-C. Wong, and C. T.-C. Nguyen, "VHF free-free beam high-Q micromechanical resonators," *J. Microelectromech. Syst.*, vol. 9, no. 3, pp. 347–360, Sep. 2000.
- [5] D. W. Car, S. Evoy, L. Sekaric, H. G. Craighead, and J. M. Parpia, "Measurement of mechanical resonance and losses in nanometer scale Silicon wires," *Appl. Phys. Lett.*, vol. 75, no. 7, pp. 920–922, Aug. 1999.
- [6] Z. Hao, A. Erbil, and F. Ayazi, "An analytical model for support loss in micromachined beam resonators with in-plane flexural vibrations," *Sens. Actuators A, Phys.*, vol. 109, pp. 156–164, Dec. 2003.
- [7] S. Pourkamali and F. Ayazi, "SOI-based HF and VHF single-crystal silicon resonators with sub-100 nm nanometer vertical capacitive gaps," in *Proc. Transducers'03*, pp. 837–840.
- [8] M. A. Abdelmoneum, M. U. Demirci, and C. T.-C. Nguyen, "Stemless wine-glass-mode disk micromechanical resonators," in *Proc. MEMS'03*, Kyoto, Japan, Jan. 2003, pp. 698–701.
- [9] A. E. H. Love, *A Treatise on the Mathematical Theory of Elasticity*, 4th ed. New York: Dover, 1944, pp. 497–498.
- [10] M. Onoe, "Contour vibrations of isotropic circular plates," *J. Acoust. Soc. Amer.*, vol. 28, no. 6, pp. 1158–1162, Nov. 1956.
- [11] S. S. H. Chen, "Extensional vibration of thin plates of various shapes," *J. Acoust. Soc. Amer.*, vol. 58, no. 4, pp. 828–831, Oct. 1975.
- [12] N. H. Farag and J. Pan, "Modal characteristics of in-plane vibration of circular plates clamped at the outer edge," *J. Acoust. Soc. Amer.*, vol. 113, no. 4, pp. 1935–1946, 2003.
- [13] L. D. Landau and E. M. Lifshitz, *Theory of Elasticity*. New York: Pergamon, 1959.
- [14] J. Kim, D.-I. Cho, and R. S. Muller, "Why Is (111) Silicon a better mechanical material for MEMS," in *Proc. Transducers 2001*, Munich, Germany, June 2001, pp. 662–665.
- [15] M. H. Toorani and A. A. Lakis, "General equations of anisotropic plates and shells including transverse shear deformations, rotary inertia and initial curvature effects," *J. Sound Vibration*, vol. 237, pp. 561–615, 2000.
- [16] R. A. Johnson, *Mechanical Filters in Electronics*. New York: Wiley, 1983.
- [17] D. L. DeVoe, "Piezoelectric thin film micromechanical beam resonators," *Sens. Actuators A, Phys.*, vol. 88, pp. 263–272, 2001.
- [18] A. Prak, M. Elwenspoek, and J. H. Fluitman, "Selective mode excitation and detection of micromachined resonators," *J. Microelectromech. Syst.*, vol. 1, no. 4, pp. 179–186, Dec. 1992.
- [19] P. R. Belanger, E. L. Adler, and N. C. Rumin, *Introduction to Circuits with Electronics*. New York: Rinehart, Winston, Holt, 1985.
- [20] R. Hull, *Properties of Crystalline Silicon*. London, U.K.: INSPEC, 1999.
- [21] W. N. Sharpe Jr., M. A. Eby, and G. Coles, "Effect of temperature on mechanical properties of polysilicon," in *Proc. Transducers'01*, pp. 1366–1369.
- [22] H. J. Meskinin, "Measurement of elastic constants at low temperature by means of ultrasonic waves data for silicon and germanium single crystals and for fused silica," *J. Appl. Phys.*, vol. 24, pp. 988–997, 1953.
- [23] K. H. Hellwidge, Ed., *Landolt-Bornstein Numerical Data and Functional Relationships Science and Technology*. ser. New Series, Germany: Springer Verlag, 1979, vol. 17 and 22.
- [24] J. J. Hall, "Electronic effects in the elastic constants of n-type silicon," *Phys. Rev.*, vol. 161, no. 3, pp. 756–761.
- [25] M. Biel, G. Brandl, and R. T. Howe, "Young's modulus of in situ phosphorus-doped polysilicon," in *Proc. 8th Int. Conf. Solid-State Sensors and Actuators*, Stockholm, Sweden, June 25–29, 1995, pp. 80–83.



Zhili Hao received the B.S. and M.S. degrees in mechanical department from Shanghai Jiao Tong University, Shanghai, P.R. China, in 1994 and 1997, respectively. She received the Ph.D. degree from the University of Central Florida, Department of Mechanical, Materials, and Aerospace Engineering, in 2000. The Ph.D. project was the research and development of a MEMS-based cooling system for microelectronics.

From 2001 to 2002, she worked as a MEMS Engineer with Nanovation Technologies, Inc., Northville, MI, and MEMS Optical, Inc., Huntsville, AL. She was involved in the development of various MEMS products, including electrostatic torsion mirrors, membrane, and piston-type mirrors, microfluidic devices for biomedical and cooling application. She is currently a Postdoctoral Fellow with School of Electrical and Computer Engineering, Georgia Institute of Technology. Her research interests are in the development of MEMS devices and studying fundamental physical mechanisms in MEMS resonant devices, such as support loss and thermoelastic damping.

Dr. Hao is a Member of the American Society of Mechanical Engineers (ASME).



Siavash Pourkamali (S'03) received the B.S. degree in electrical engineering from Sharif University of Technology, Iran, in 2001 and the M.S. degree from Georgia Institute of Technology, Atlanta, in 2004. Currently he is pursuing the Ph.D. degree in Electrical Engineering Department, Georgia Institute of Technology.

His main research interests are in the areas of RF MEMS resonators and filters, silicon micromachining technologies, and integrated microsystems.



Farrokh Ayazi (S'96–M'99) was born in February 19, 1972. He received the B.S. degree in electrical engineering from the University of Tehran, Iran, in 1994 and the M.S. and the Ph.D. degrees in electrical engineering from the University of Michigan, Ann Arbor, in 1997 and 2000, respectively. He joined the faculty of Georgia Institute of Technology in December 1999, where he is currently an Assistant Professor in the School of Electrical and Computer Engineering. His current research interests are in the areas of low and high frequency micro- and nanoelectromechanical resonators, VLSI analog integrated circuits, MEMS inertial sensors, and microfabrication technologies.

Prof. Ayazi is a 2004 recipient of the NSF CAREER award, the 2004 Richard M. Bass Outstanding Teacher Award, and the Georgia Tech. College of Engineering Cutting Edge Research Award for 2001–2002. He received a Rackham Predoctoral Fellowship from the University of Michigan for 1998–1999.